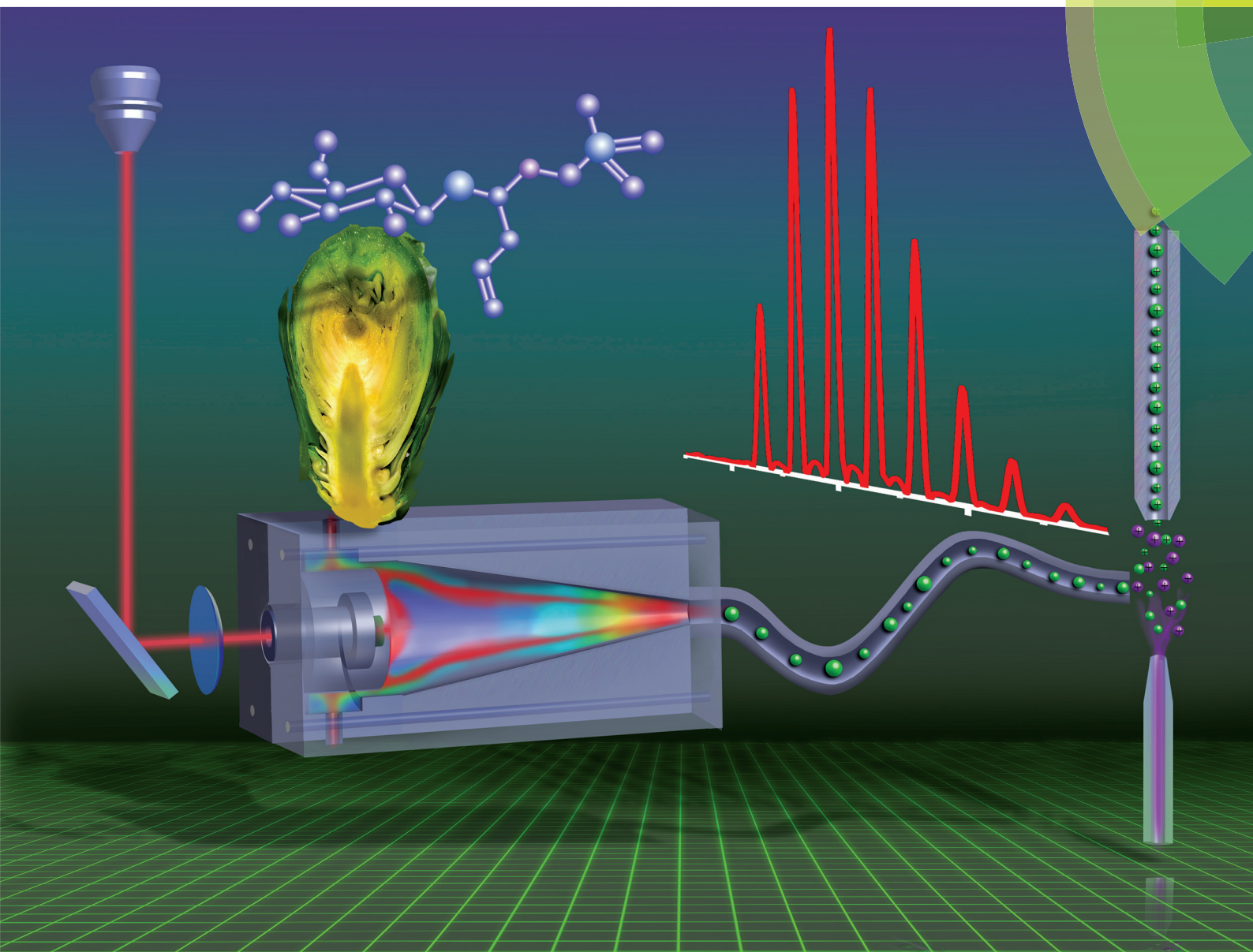


Analyst

rsc.li/analyst



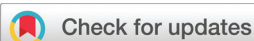
ISSN 0003-2654



PAPER

Akos Vertes *et al.*

Enhanced sensitivity and metabolite coverage with remote laser ablation electrospray ionization-mass spectrometry aided by coaxial plume and gas dynamics



Cite this: *Analyst*, 2017, **142**, 3157

Enhanced sensitivity and metabolite coverage with remote laser ablation electrospray ionization-mass spectrometry aided by coaxial plume and gas dynamics†

Jarod A. Fincher,^a Andrew R. Korte,^a Brent Reschke,^b Nicholas J. Morris,^b Matthew J. Powell^b and Akos Vertes  ^{*a}

Laser ablation electrospray ionization-mass spectrometry (LAESI-MS) allows for direct analysis of biological tissues at atmospheric pressure with minimal to no sample preparation. In LAESI, a mid-IR laser beam ($\lambda = 2.94 \mu\text{m}$) is focused onto the sample to produce an ablation plume that is intercepted and ionized by an electrospray at the inlet of the mass spectrometer. In the remote LAESI platform, the ablation process is removed from the mass spectrometer inlet and takes place in an ablation chamber, allowing for incorporation of additional optics for microscopic imaging and targeting of specific features of the sample for laser ablation sampling. The ablated material is transported by a carrier gas through a length of tubing, delivering it to the MS inlet where it is intercepted and ionized by an electrospray. Previous proof-of-principle studies used a prolate spheroid ablation chamber with the carrier gas flow perpendicular to the ablation plume. This design resulted in significant losses of MS signal in comparison to conventional LAESI. Here we present a newly designed conical inner volume ablation chamber that radially confines the ablation plume produced in transmission geometry. The carrier gas flow and the expanding ablation plume are aligned in a coaxial configuration to improve the transfer of ablated particles. This new design not only recovered the losses observed with the prolate spheroid chamber design, but was found to provide an ~12–15% increase in the number of metabolite peaks detected from plant leaves and tissue sections relative to conventional LAESI.

Received 15th May 2017,

Accepted 27th June 2017

DOI: 10.1039/c7an00805h

rsc.li/analyst

Introduction

The field of ambient ionization mass spectrometry (MS) has expanded rapidly over the last decade, with widespread applications in fields such as explosives detection, surface chemistry, pharmaceutical analysis, forensics, metabolomics, and biological imaging.^{1–5} In biological analysis, ambient ionization allows for direct analysis of tissues with minimal to no sample preparation, permitting investigation into the native state of the system.⁶ Currently, ambient ionization platforms such as desorption electrospray ionization (DESI), direct analysis in real time (DART), laser ablation electrospray ionization (LAESI), rapid evaporative ionization mass spectrometry (REIMS), and SpiderMass among many others allow for direct analysis of biological tissues.^{7–11}

In spite of the development of these novel techniques, applications of ambient ionization MS are often limited by the physical constraints of sampling. Often, the sample must be brought near to the inlet of the mass spectrometer for analysis, resulting in inherent geometric limitations for the complexity of the sampling system. Recent efforts have sought to overcome this through remote sampling, where the sample is removed from the mass spectrometer inlet. For example, the recently developed iKnife technology allows for real time MS analysis of tissues during surgery. In the iKnife configuration, material vaporized by an electrosurgical instrument is transferred to the inlet of an MS system and multivariate analysis of the resulting spectra allows discrimination of tissue types, permitting the determination that tissue of a given type (*e.g.*, tumour) has been removed.¹²

An inherent limitation of remote sampling MS platforms is a loss of molecular coverage and sensitivity due to transport losses. For example, transported ions can be lost to ion–ion interactions and ion–neutral interactions, yielding reduced intensities and loss of chemical information.^{13–15} In laser ablation sampling, some of the ablated material is lost due to redeposition onto the sample, ablation chamber, or transfer tubing, and the transport efficiency depends upon factors

^aDepartment of Chemistry, The George Washington University, Washington, DC 20052, USA. E-mail: vertes@gwu.edu; Fax: +1 (202) 994-5873; Tel: +1 (202) 994-2717

^bProtea Biosciences, 1311 Pineview Drive, Suite 501, WV 26505, USA

†Electronic supplementary information (ESI) available. See DOI: 10.1039/c7an00805h

including the pressure drop, gas velocity, inner diameter of transfer tubing, and radial diffusion.^{15–18} The effect of carrier gas choice on the particle size distribution has been extensively demonstrated for laser ablation inductively coupled plasma (ICP) MS.^{19,20} Carrier gas dynamics and aerosol transport in these systems have been described by both modelling and through experiments.^{21,22}

Existing remote sampling MS systems use a variety of material transport mechanisms. For example, REIMS uses a Venturi pump installed at the distal end of the transfer tube, where a differentially-pumped intermediate pressure chamber houses a jet separator combined with a cylindrical electrostatic lens to focus ions into the inlet of the mass spectrometer. A Venturi pump is also utilized in the remote DESI platform, aspirating off the desorbed ions and transferring them over a distance of ~1 m. In SpiderMass, a tissue is ablated by a $\lambda = 2.94 \mu\text{m}$ laser and the ions are transported to the mass spectrometer inlet through aspiration.

The platforms discussed above (REIMS, remote DESI, and SpiderMass) use aspiration for efficient transfer of ions generated during the sampling process to the MS inlet for analysis. However, there have also been several novel remote sampling platforms that incorporate a continuously flowing solvent in place of a carrier gas to effectively capture and transport the ablated material. For example, a UV laser microdissection system was coupled to a liquid-vortex probe that captured the ablated material and transferred it to an electrospray ion source for MS analysis.^{23,24} In another system based on mid-IR laser ablation, the ablation plume is captured by a solvent that is coupled to high-performance chemical separation techniques, such as liquid chromatography and capillary electrophoresis.^{25,26}

In remote LAESI, which also uses a laser beam with $\lambda = 2.94 \mu\text{m}$ to ablate water-rich biological tissues, a nonreactive carrier gas (*e.g.*, N_2) is used to entrain and transfer ablated neutrals to the inlet of the MS where this material is intercepted by an electrospray. The incorporation of this electrospray allows for enhanced sensitivity and molecular coverage by generating ions from neutrals within the ablated droplets.

In this work, we present an ablation chamber design that significantly improves the entrainment and transfer efficiency of the ablated material compared to earlier remote LAESI and conventional LAESI experiments. In this new design, a sample is ablated in transmission geometry within a conical inner volume ablation chamber. A gas flow coaxial to the ablation plume provides radial confinement of the ejected material. These modified gas dynamics lead to a significant enhancement in sampling efficiency, resulting in a greater sensitivity and molecular coverage relative to previous remote and conventional LAESI configurations.

Experimental

Chemicals and sample preparation

Methanol (A452-4), chloroform (C607-4), and water (W6-212), were purchased from Alfa Aesar (Ward Hill, MA, USA) at HPLC-

grade. Verapamil hydrochloride (J61535) was purchased from Sigma-Aldrich (St Louis, MO, USA). Glacial acetic acid (A35-500) was purchased from Fisher Scientific (Waltham, MA, USA). Verapamil standards used for limit of detection (LOD) studies were prepared by serial dilution in HPLC-grade water immediately prior to analysis.

Ablation chamber and transfer tubing

The conical inner volume ablation chamber was designed in SolidWorks 2014 (Dassault Systèmes, Vélizy-Villacoublay, France) and 3D printed as described previously.²⁷ Briefly, the chamber structure was produced by a 3D printer (Fortus 400 mc, Proto3000, Vaughan, Ontario, Canada) using a T10 tip and acrylonitrile butadiene styrene (ABSM30) as the structural material. SR30 support material was delivered by a T12SR20/30 tip and subsequently removed by sonicating for 2 hours in a WaterWorks soluble concentrate bath (P4000SC). All materials used for printing were purchased from Stratasys (Eden Prairie, MN, USA).

For transfer tubing in remote LAESI analysis, Tygon stock (E-3603, U.S. Plastic Co., Lima, OH, USA) was used because of its lack of phthalate plasticizers, which could contribute significant MS background.²⁸ The 60 cm long transfer tube was held straight and in line with the ablation chamber axis and intersected the emitter-MS inlet axis at a right angle. Under the optimized gas flow rate conditions, the electrospray droplet trajectories were not affected significantly by the gas exiting the transfer tube. The tube exit-emitter geometry was defined by the distance of the tube end from the electrospray axis (8 mm), and by the distance of the emitter tip from the tube axis (2 mm). In contrast, in the conventional LAESI geometry the sample was placed approximately 12–14 mm away from the electrospray axis, and the laser beam was positioned at 5 mm in front of the emitter tip. The 60 cm tube length enabled the future implementation of a research-grade microscope to hold the ablation chamber. Preliminary measurements had shown that increasing the length of the transfer tube resulted in a signal loss. The selected transfer tube length represented a tradeoff between engineering and signal strength considerations. All geometric parameters were individually optimized prior to the comparison of remote and conventional LAESI sources. Illustrations of the previous and redesigned ablation chambers and the overall experimental setup are presented in Fig. 1.

Electrospray, laser, and mass spectrometer

The homebuilt ion source used for conventional and remote LAESI-MS analysis has been described in detail previously.^{9,27} Briefly, a Nd:YAG laser-based optical parametric oscillator (Vibrant IR, Oportek, Carlsbad, CA) with 4 ns pulse width and 10 Hz repetition rate was focused onto the sample with a 100 mm focal length CaF_2 plano-convex lens (LA5817, Thorlabs, NJ, USA), producing a laser spot size of ~300 μm . This spot size was selected to test the chamber, and it did not represent a limitation for spatial resolution. In a recent study, we have demonstrated 10–20 μm ablation spot sizes with a reflective objective.²⁹ A syringe pump (Physio 22, Harvard

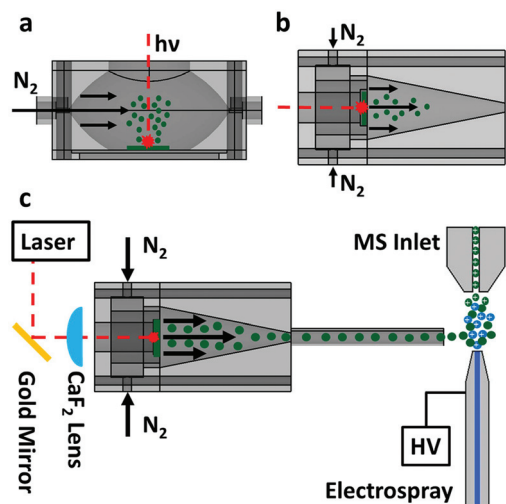


Fig. 1 (a) Prolate spheroid ablation chamber design illustrating gas flow perpendicular to laser induced sample ablation plume expansion. (b) Conical inner volume ablation chamber illustrating gas flow coaxial to laser induced sample ablation plume expansion. (c) Schematic of remote LAESI with conical inner volume ablation chamber interfaced to a mass spectrometer. Sample is mounted on a quartz cover slip in focal plane of CaF_2 lens to achieve transmission geometry ablation.

Apparatus, Holliston, MA, USA) supplied the electro spray solution (1 : 1 methanol : water containing 0.1% glacial acetic acid for positive mode; 2 : 1 methanol : chloroform containing 0.1% glacial acetic acid for negative mode) at 400 nL min^{-1} through a stainless steel emitter (MT320-100-5-5, i.d. $100 \mu\text{m}$, New Objective, Woburn, MA, USA). A high voltage power supply (PS350, Stanford Research Systems, Sunnyvale, CA, USA) provided a DC voltage of -2600 V in negative ion mode and $+3500 \text{ V}$ in positive ion mode. All LAESI-MS spectra were acquired using a Q-TOF Premiere mass spectrometer (Waters Co., Milford, MA, USA) and analyzed within the MassLynx software package (version 4.1, Waters Co., Milford, MA, USA). For identification of metabolites from plant tissues, collision induced dissociation (CID) MS/MS spectra were acquired at 20–25 eV.

Computational fluid dynamic modelling

The Navier–Stokes equations (conservation of mass, momentum, and energy) were solved to determine gas velocity, density, and temperature distributions, and distinguish laminar and turbulent flows. Computational fluid dynamic (CFD) modelling was performed using the CFD solver module of SolidWorks (Flow Simulation 2015, Dassault Systèmes, Vélizy-Villacoublay, France) for the gas dynamics inside the prolate spheroid and conical inner volume ablation chambers. The numerical solutions were sought through the finite volume method using a locally refined adaptive mesh. The carrier gas was modelled as a steady-state flow field. Convergence conditions were set as four travels of gas volume elements through the chamber. Mach numbers, calculated in the peak flow rate regions, indicated that the flow was subso-

nic throughout both chambers. The carrier gas was treated as an ideal gas in the simulations.

Boundary conditions were defined for the gas inlets and outlets of the two chambers (see Fig. 2a and 3a). The outlet was held at constant environmental pressure for both chambers. Inlet boundary conditions were entered as mass flow rates calculated from the experimentally observed optimal volumetric flow rates. No-slip boundary conditions were placed along the inner walls of the chambers.

For the simulations of particle trajectories, the cylindrically symmetric ablation plume expanding in the carrier gas was modelled as a two-phase flow of uniform $5 \mu\text{m}$ particles originating from a single point on the quartz coverslip (indicated by light blue in Fig. 4), representing the focal spot, and diverging in a semicircular geometry in the x - y plane with an initial velocity of 150 m s^{-1} . When determining the particle trajectories, it was assumed that the ablation plume had an overall negligible influence on the carrier gas flow. The drag coefficient of the particles was calculated using Henderson's formula.³⁰ Ideal particle reflection was applied as a boundary condition along the inner walls of the chambers. These parameters were chosen based on experimental observations of mid-IR laser induced ablation plume dynamics.^{31–33}

Standards and biological samples

Verapamil solutions at different concentrations in $5 \mu\text{L}$ aliquots were deposited onto a quartz cover slip and completely ablated.

Six-week old wildtype *Arabidopsis thaliana* plants were grown in the laboratory. Seeds were sown on soil and cold treated for 48 hours at $4 \text{ }^\circ\text{C}$. Seedlings were grown at $22 \text{ }^\circ\text{C}$,

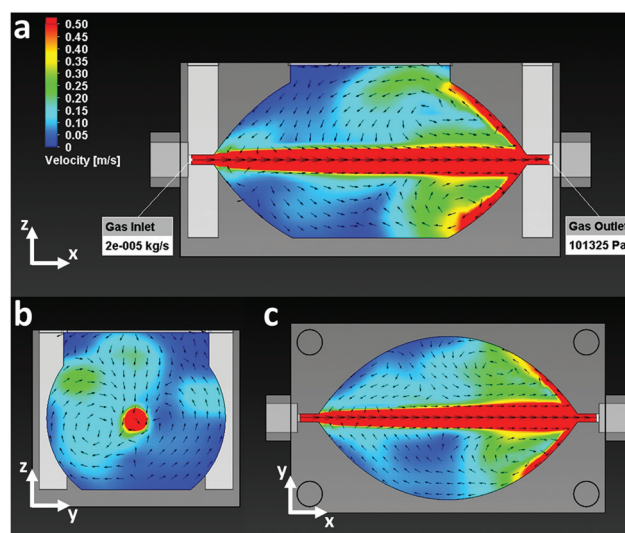


Fig. 2 CFD modelling of nitrogen carrier gas dynamics inside proof-of-principle prolate spheroid ablation chamber. Velocity contour plots with vectors illustrating gas flow trajectories throughout chamber. (a) Side view of the chamber at midplane with the sample at the bottom and the ablation laser introduced from the top. (b) End-on view of the chamber at the midpoint between gas inlet and outlet. (c) Top-down view of the chamber in the plane of the gas inlet at left and outlet at right.

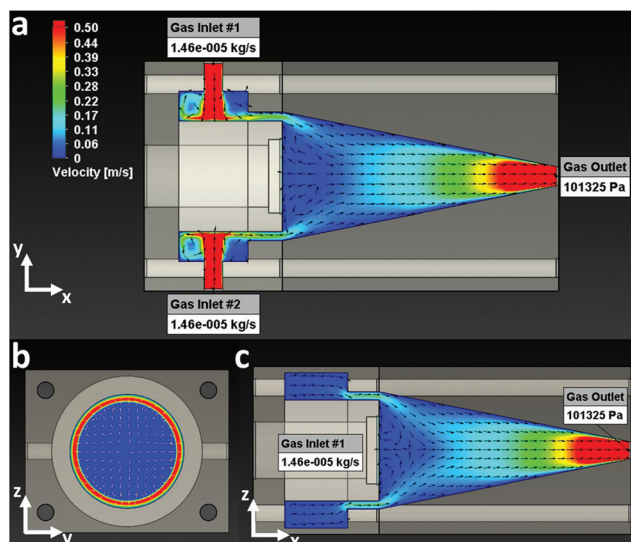


Fig. 3 CFD modelling of nitrogen carrier gas dynamics inside conical inner volume ablation chamber. Velocity contour plots with vectors illustrating gas flow trajectories throughout chamber. (a) Axial midplane view showing the inlets of the chamber and the ablation laser introduced in a transmission geometry from the left. (b) End-on view of the chamber illustrating annular flow within the conical region just in front of the sample plane. (c) Axial midplane view of the chamber perpendicular to the inlets and the ablation laser introduced in a transmission geometry.

65% relative humidity, under short-day conditions (8-hour light exposure at $125 \mu\text{mol m}^{-2} \text{s}^{-1}$). The plants were then raised for two weeks at $22 \text{ }^\circ\text{C}$ with daily 12-hour light exposure (average $14 \mu\text{mol m}^{-2} \text{s}^{-1}$). At eight weeks, healthy *A. thaliana* plant leaves were cut from the stem and analyzed immediately.

Brussels sprouts (*Brassica oleracea*) were obtained from a local supermarket. The buds were placed inside a cryostat chamber (CM1800, Leica Microsystems Inc., Nussloch, Germany) at $-20 \text{ }^\circ\text{C}$ and mounted to a sectioning chuck using a few drops of water. After one hour, $60 \mu\text{m}$ thick tissue sections were cut and thaw-mounted to 0.5 mm thick quartz coverslips (Ted Pella Inc., Redding, CA, USA).

Results and discussion

Conical ablation chamber with coaxial flow

A simplified schematic illustrating the gas flow profiles of the original and redesigned remote LAESI chambers can be found in Fig. 1. Redesign of the chamber for ablation in a transmission geometry allowed for the coaxial orientation of the ablation plume and the carrier gas flow. This was a major departure from the previous prolate spheroid design (see Fig. 1a and b), where material must be redirected 90° to be entrained in the exiting gas flow. This coaxial orientation of the ablation plume and carrier gas, in conjunction with the radial compression introduced by the conical taper of the chamber, was expected to significantly improve entrainment and transfer efficiency of ablated material.

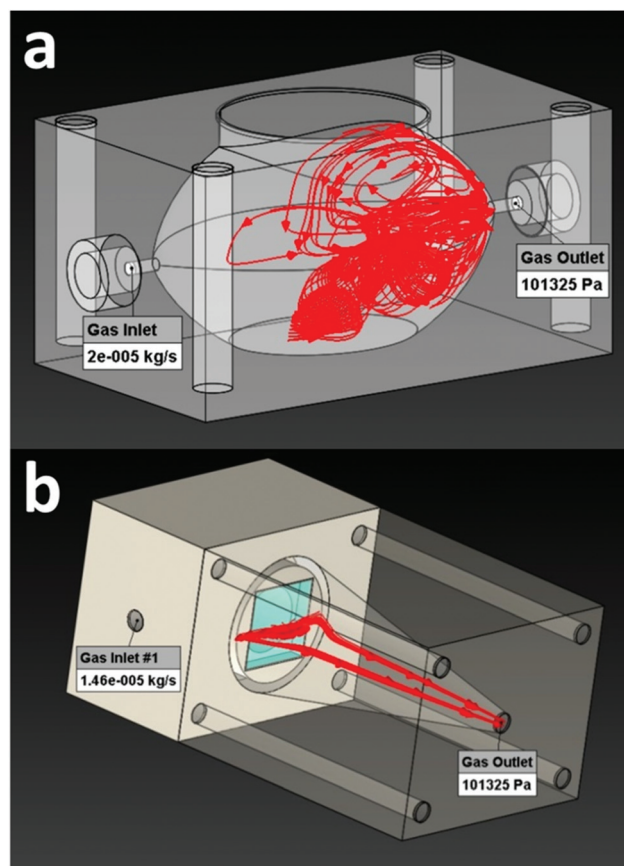


Fig. 4 Three-dimensional view of particle trajectories (red lines and arrows) inside (a) a prolate spheroid chamber and (b) conical inner volume chamber with ideally reflecting walls.

The chamber volumes for the conical and the prolate spheroid chambers were calculated by SolidWorks as 25.0 and 25.6 cm^3 , respectively, and the corresponding transfer tube volumes were 4.2 and 7.4 cm^3 , respectively. Thus, the total volumes of the two chamber-tube assemblies were 29.2 and 33.0 cm^3 , respectively. To ensure adequate space for entrainment of ablated particles, a conical geometry with an axial length of 6 cm was implemented. This length was chosen based on the stopping distance of the droplets in the ablation plume (where the atmospheric drag force stops the ablated material), which had been observed to be approximately 3 cm in resting background gas.³² The chosen dimensions provide sufficient space for the particles to decelerate to the carrier gas velocity, and prevent attachment of the ablated material onto the chamber walls, promoting entrainment and transport.

The diameter of the chamber outlet was increased from 1 mm in the original prolate spheroid chamber to 4 mm in the conical inner volume chamber. This modification led to a reduction in the Reynolds number within this part of the chamber from ~ 1400 to ~ 500 , promoting more robust laminar flow and transfer of entrained particulates.

For the redesigned chamber, the efficiency of sample transport through the transfer tube was also investigated as a func-

tion of diameter and gas flow rate. A 3 mm ID transfer tube was found to provide the greatest transfer efficiency at a flow rate of 1.5 L min^{-1} . The calculated Reynolds number for gas flow inside the transfer tube was ~ 700 , well below the threshold for turbulent flow. Furthermore, the use of a smaller ID transfer tube increases the cross-sectional overlap between the electrospray and transferred particulates at the MS inlet, which is expected to lead to higher ion yields from the ablated material. The relative position of the transfer tube outlet and the electrospray emitter has also been optimized to produce the highest ion signal.

Modelled gas dynamics

To evaluate whether the proposed modifications (coaxial gas flow through an annular inlet, and conical inner geometry) would lead to enhanced entrainment of laser induced particulates, the two chambers were compared *in silico* using the CFD software. Velocity contour plots displaying carrier gas dynamics inside the original prolate spheroid ablation chamber in three orthogonal cross-sectional planes can be found in Fig. 2. Fig. 2a shows that the gas velocity is highest along a narrow path of flow travelling from inlet to outlet. As the gas flow travels through the chamber, a slight radial expansion of the flow profile occurs before reaching the outlet. The gas velocity gradually decreases along this line, with significantly reduced velocity just before the outlet. Fig. 2c reveals Eddy currents near the outlet of the chamber, produced as a result of the increased backpressure at the outlet interface. As the divergent gas flow reaches the outlet wall, the chamber's inner geometry and small outlet diameter (1 mm) prevent the gas from being evacuated efficiently. Consequently, the gas flow is redirected back towards the inlet, leading to potentially turbulent flow regimes inside the chamber and preventing optimal transfer of material.

In Fig. 3 there are three analogous velocity contour plots for the new conical inner volume ablation chamber. As predicted, incorporation of the conical inner geometry led to confinement and focusing of gas flow through the chamber. Fig. 3a shows an axial midplane view showing the inlets of the chamber with gas flow entering through the two antipodal inlets and being partially dispersed within the front compartment before entering the conical region. Fig. 3b highlights the annular gas flow adjacent to the chamber wall just in front of the sample plane. This relatively high velocity gas flow along the wall helps to capture divergent ablated material and minimizes deposition onto the chamber wall. Fig. 3c shows the axial midplane view of the chamber perpendicular to the inlets, highlighting rotational uniformity of the gas flow entering the conical region and its convergence toward the exit.

Ablation particle trajectory simulations

To evaluate the impact of the modified gas dynamics on particle transfer efficiency, particle trajectory simulations were performed. A 3-D rendered view of both chambers with the particle trajectories can be found in Fig. 4 and the combined views of the gas velocity contour plots and particle trajectories

are depicted in Fig. S3.† Fig. 4a shows the prolate spheroid chamber with 37 particles departing from the bottom showing a uniform angular distribution in the axial midplane. The turbulent gas flow within the prolate spheroid chamber causes the majority of generated particles to be distributed throughout the chamber rather than directly extracted *via* the outlet (Fig. 4a), yielding a simulated transfer efficiency of only 3% in case of perfectly adsorbing walls and 32% in case of ideally reflecting walls. Fig. 4b shows the conical inner volume chamber with particles departing from the ablation platform showing a uniform angular distribution in the plane of the gas inlets. Simulated particle trajectories largely mirror the gas flow depicted in Fig. 3a. Tallying the particles that leave through the outlet in Fig. 4b shows efficient capture and entrainment within the conical inner volume chamber, leading to a simulated transfer efficiency of 81% in case of perfectly adsorbing walls and 100% in case of ideally reflecting walls. The actual retention of the particles on the walls is unknown but it falls between these two limiting cases.

Annular gas flow is produced by a recessed cylindrical gas distribution volume surrounding the ablation region. This laminar gas flow merges with the expanding ablation plume and guides the particulates toward the axis of the chamber. With the sample placed in the centre of the annular gas flow, it is not displaced even at high gas velocities. This allows for the use of higher carrier gas flow rates and results in enhanced transfer efficiency for the ablated material.

Adjustment of the gas flow rate allowed for efficient capture and extraction of the material from the ablation chamber. While the laser ablation process creates a shock wave and turbulent flow of the ablated material, the annular coaxial gas flow allows for capture of the droplets in the plume once their velocity has decreased to match that of the carrier gas.

Experimental figures of merit

A comparison of verapamil ion yields from standard solutions for conventional reflection geometry and remote LAESI (both in prolate spheroid and conical ablation chambers) can be found in Fig. 5. The comparative analysis showed significantly improved sensitivity for the conical chamber compared to the prolate spheroid geometry, and at high loadings even compared to conventional LAESI. The magnitude of improvement using the new geometry is consistent with the 3 to 27-times higher calculated transfer efficiency in the conical chamber. The LOD for the conical chamber is estimated to be 8 pmol. Above 10 pmol, the signal from the conical chamber exceeds that from conventional LAESI but the latter shows lower LOD and extended dynamic range to lower loadings. We speculate that the signal loss at lower loadings can be attributed to analyte retention at the surfaces of the inner walls of the chamber and transfer tubing. In particular, the ABSM30 chamber material has significant surface roughness and some level of innate porosity. If this structure acts as a saturable adsorber for the analyte at a 4 pmol loading the sharp drop in the signal can be rationalized. A dynamic range of two orders of magnitude was observed for the remote LAESI platform.

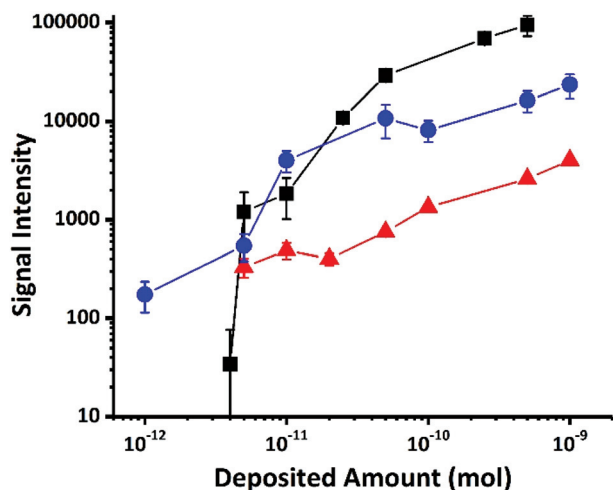


Fig. 5 Comparison of verapamil signal intensities as a function of analyte loading for conventional LAESI-MS (●), and remote LAESI-MS using conical (■) and prolate spheroid (▲) inner volume ablation chamber designs.

To explore the aerosol elution times, the temporal profile of the total ion count following single laser shots was compared between the conical inner volume chamber and conventional LAESI. The signal per laser shot for the conical inner volume chamber persisted for 3 s with 31% RSD, whereas it lasted for 2 s with 53% RSD for conventional LAESI. The temporal variations of peaks for selected ions in the mass spectra were approximated by lognormal distributions (see Fig. S1†). Conventional LAESI signal showed a slightly faster response and lasted for a somewhat shorter time. The FWHM for conventional LAESI at m/z 455.29 was 0.8 s, whereas it was 1.1 s at m/z 381.06 for the conical chamber.

Remote LAESI of metabolites in plant samples

To demonstrate the utility of remote LAESI for biological analysis, eight-week old *Arabidopsis thaliana* plant leaves and 60 μm thick Brussels sprout (*Brassica oleracea*) bud sections were analysed. These biological samples were chosen for the known presence of glucosinolates in them.³⁴ Glucosinolates are secondary metabolites that act as defence compounds in plants to protect them against herbivore attacks. Recently, they have drawn interest from the medical community for their ability to reduce cancer risks.^{35,36}

To accurately compare the molecular coverage obtained from conventional LAESI and the conical geometry remote ablation chamber, in both cases a total of 100 laser shots were fired per sample, corresponding to 10 laser shots per MS scan. The laser spot sizes and shapes in the conventional and remote LAESI with conical ablation chamber were kept the same. For conventional LAESI analysis, a laser fluence of 3.2 J cm^{-2} was found to provide the optimal signal intensity. In remote LAESI analysis, a laser fluence of 4.3 J cm^{-2} provided the strongest signal. The spectra were background subtracted in MassLynx to minimize the electrospray-related peaks and deisotoped using mMass software, and the total number of

peaks was calculated.³⁷ The analysis of *Arabidopsis* leaves yielded 101 sample related peaks detected by remote LAESI and 88 detected by conventional LAESI (see Fig. S2a†). A total of seven glucosinolates ((1) glucoerucin, (2) glucoraphanin, (3) glucobrassicin, (4) 7-methylthioheptyl glucosinolate, (5) 8-methylthiooctyl glucosinolate, (6) neoglucobrassicin, and (7) glucohirsutin) were detected in *Arabidopsis* leaves using both remote and conventional LAESI (see Fig. 6a) with sufficient ion intensities for confirmatory MS/MS measurements (for the identification see an example in Fig. 6b and ESI Table S1†). These assignments coincide with previous glucosinolate assignments from *Arabidopsis*.³⁴

In the analysis of Brussels sprout bud sections, after background subtraction and deisotoping 161 peaks were detected

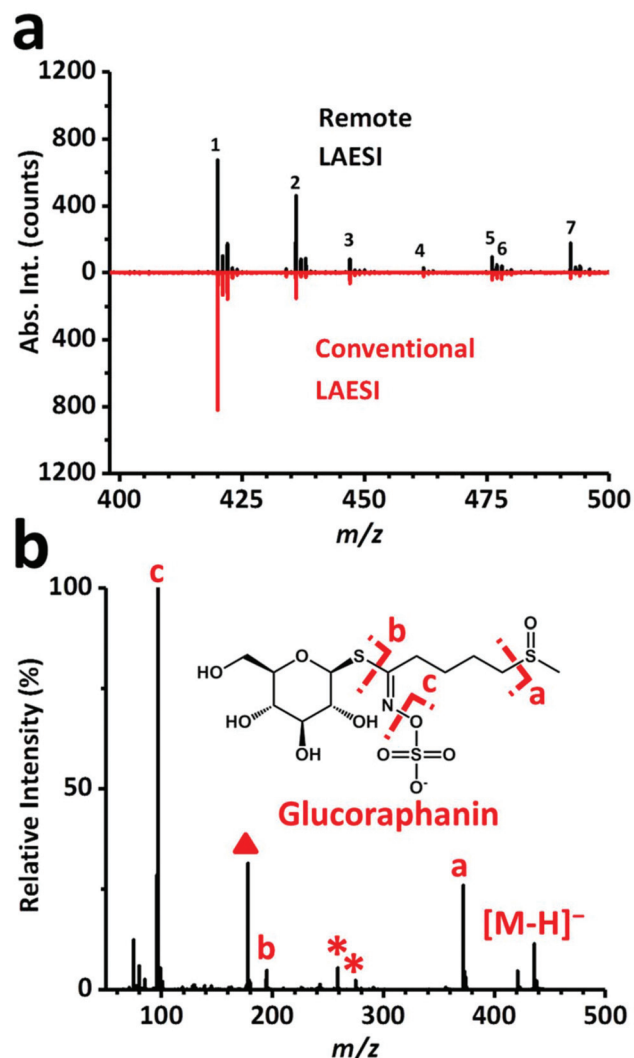


Fig. 6 (a) Glucosinolate region of negative ion mode spectra obtained from *Arabidopsis thaliana* leaves using conical inner volume remote LAESI-MS and conventional LAESI-MS. Seven annotated glucosinolates, (1) glucoerucin, (2) glucoraphanin, (3) glucobrassicin, (4) 7-methylthioheptyl glucosinolate, (5) 8-methylthiooctyl glucosinolate, (6) neoglucobrassicin, and (7) glucohirsutin, were identified by tandem MS. (b) Tandem MS of peak (2) confirmed its assignment as glucoraphanin.

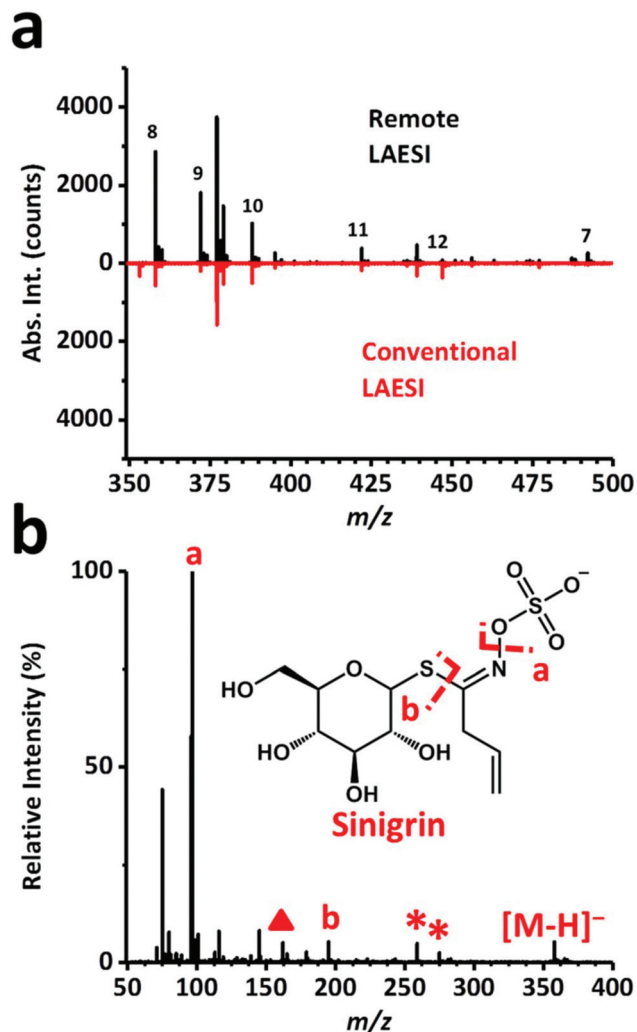


Fig. 7 (a) Glucosinolate region of negative ion mode spectra obtained from 60 μm thick Brussels sprout bud section using conical inner volume remote LAESI-MS and conventional LAESI-MS. Six glucosinolates, (7) glucohirsutin, (8) sinigrin, (9) gluconapin, (10) progoitrin, (11) glucoiberin, and (12) glucobrassicin, were identified by tandem MS. (b) Tandem MS of peak (8) confirmed its assignment as sinigrin.

by remote LAESI using the conical ablation chamber and 144 by conventional LAESI (see Fig. S2b[†]). For both platforms, six glucosinolates ((7) glucohirsutin, (8) sinigrin, (9) gluconapin, (10) progoitrin, (11) glucoiberin, and (12) glucobrassicin) were detected (see Fig. 7a and ESI Table S2[†]) and the confirmation of their assignments was performed *via* MS/MS. The tandem MS identification of sinigrin in a Brussels sprout bud section is shown in Fig. 7b. In agreement with previous studies, this was the dominant glucosinolate signal in Brussels sprouts.³⁸

Conclusions

Incorporation of coaxial gas flow and radial confinement of the laser induced ablation plume within a conical inner volume ablation chamber was found to significantly improve the trans-

fer efficiency of the remote LAESI-MS platform. This improvement in transfer efficiency provided molecular coverage for non-targeted analysis of biological samples that is comparable or superior to the conventional LAESI-MS configuration.

The work presented here clearly demonstrates the ability of remote LAESI to achieve sufficient sensitivity for detection and identification of targeted metabolites, *e.g.*, glucosinolates, from plant tissues. Future work will seek to further enhance the sensitivity and molecular coverage of remote LAESI by expanding CFD modelling to test additional chamber geometries and individually optimize dimensions and design elements, as well as to reduce the aerosol elution times. The ability to model various particle sizes and velocities, carrier gas flow rates and compositions, and geometric factors and to examine their influence on transfer efficiency provides the foundation for the optimal design of remote sampling platforms, including those used in laser ablation sampling for ICP-MS. Furthermore, we envision that this work will eventually allow high-spatial resolution chemical and optical imaging at atmospheric pressure, by incorporating a high-quality optical imaging system and a sample cooling element to prevent dehydration of the tissue sample by the carrier gas flow during long imaging acquisitions.

Acknowledgements

The authors acknowledge financial support by the U.S. Department of Energy, Office of Science, Office of Basic Energy Sciences, Chemical Sciences, Geosciences, and Biosciences Division under Award DE-FG02-01ER15129, and the Office of Biological and Environmental Research under Award DE-SC0013978. Wildtype *A. thaliana* plants were generously provided by the laboratory of Professor Shunyuan Xiao and logistical arrangements were made by Qiong Zhang at the University of Maryland, College Park, MD.

References

- Z. Takats, I. Cotte-Rodriguez, N. Talaty, H. W. Chen and R. G. Cooks, *Chem. Commun.*, 2005, 1950–1952.
- H. W. Chen, N. N. Talaty, Z. Takats and R. G. Cooks, *Anal. Chem.*, 2005, 77, 6915–6927.
- D. R. Ifa, A. U. Jackson, G. Paglia and R. G. Cooks, *Anal. Bioanal. Chem.*, 2009, 394, 1995–2008.
- P. Nemes, A. A. Barton, Y. Li and A. Vertes, *Anal. Chem.*, 2008, 80, 4575–4582.
- P. Nemes and A. Vertes, *TrAC, Trends Anal. Chem.*, 2012, 34, 22–34.
- A. Venter, M. Nefliu and R. G. Cooks, *TrAC, Trends Anal. Chem.*, 2008, 27, 284–290.
- Z. Takats, J. M. Wiseman, B. Gologan and R. G. Cooks, *Science*, 2004, 306, 471–473.
- R. B. Cody, J. A. Laramee and H. D. Durst, *Anal. Chem.*, 2005, 77, 2297–2302.

- 9 P. Nemes and A. Vertes, *Anal. Chem.*, 2007, **79**, 8098–8106.
- 10 B. Fatou, P. Saudemont, E. Leblanc, D. Vinatier, V. Mesdag, M. Wisztorski, C. Focsa, M. Salzet, M. Ziskind and I. Fournier, *Sci. Rep.*, 2016, **6**, 25919.
- 11 O. Golf, N. Strittmatter, T. Karancsi, S. D. Pringle, A. V. M. Speller, A. Mroz, J. M. Kinross, N. Abbassi-Ghadi, E. A. Jones and Z. Takats, *Anal. Chem.*, 2015, **87**, 2527–2534.
- 12 J. Balog, L. Sasi-Szabo, J. Kinross, M. R. Lewis, L. J. Muirhead, K. Veselkov, R. Mirnezami, B. Dezso, L. Damjanovich, A. Darzi, J. K. Nicholson and Z. Takats, *Sci. Transl. Med.*, 2013, **5**, 194ra93.
- 13 T. C. Chen, W. Xu, S. Garimella and Z. Ouyang, *J. Mass Spectrom.*, 2012, **47**, 1466–1472.
- 14 I. Cotte-Rodriguez, C. C. Mulligan and G. Cooks, *Anal. Chem.*, 2007, **79**, 7069–7077.
- 15 S. Garimella, W. Xu, G. M. Huang, J. D. Harper, R. G. Cooks and Z. Ouyang, *J. Mass Spectrom.*, 2012, **47**, 201–207.
- 16 C. H. Chen, Z. Q. Lin, R. Tian, R. Y. Shi, R. G. Cooks and Z. Ouyang, *Anal. Chem.*, 2015, **87**, 8867–8873.
- 17 J. F. Delamora and P. Riesco-Chueca, *J. Fluid Mech.*, 1988, **195**, 1–21.
- 18 R. B. Dixon, M. S. Bereman, D. C. Muddiman and A. M. Hawkridge, *J. Am. Soc. Mass Spectrom.*, 2007, **18**, 1844–1847.
- 19 I. Horn and D. Gunther, *Appl. Surf. Sci.*, 2003, **207**, 144–157.
- 20 Z. K. Wang, B. Hattendorf and D. Gunther, *J. Am. Soc. Mass Spectrom.*, 2006, **17**, 641–651.
- 21 D. Bleiner and D. Gunther, *J. Anal. At. Spectrom.*, 2001, **16**, 449–456.
- 22 S. H. Jeong, O. V. Borisov, J. H. Yoo, X. L. Mao and R. E. Russo, *Anal. Chem.*, 1999, **71**, 5123–5130.
- 23 J. F. Cahill, V. Kertesz and G. J. Van Berkel, *Anal. Chem.*, 2015, **87**, 11113–11121.
- 24 M. Lorenz, O. S. Ovchinnikova, V. Kertesz and G. J. Van Berkel, *Rapid Commun. Mass Spectrom.*, 2013, **27**, 1429–1436.
- 25 S. G. Park and K. K. Murray, *J. Mass Spectrom.*, 2012, **47**, 1322–1326.
- 26 S. G. Park and K. K. Murray, *Rapid Commun. Mass Spectrom.*, 2013, **27**, 1673–1680.
- 27 L. R. Compton, B. Reschke, J. Friend, M. Powell and A. Vertes, *Rapid Commun. Mass Spectrom.*, 2015, **29**, 67–73.
- 28 S. S. Hill, B. R. Shaw and A. H. B. Wu, *Biomed. Chromatogr.*, 2003, **17**, 250–262.
- 29 R. S. Jacobson, R. L. Thurston, B. Shrestha and A. Vertes, *Anal. Chem.*, 2015, **87**, 12130–12136.
- 30 C. B. Henderson, *AIAA J.*, 1976, **14**, 707–708.
- 31 I. Apitz and A. Vogel, *Appl. Phys. A*, 2005, **81**, 329–338.
- 32 P. Nemes, H. H. Huang and A. Vertes, *Phys. Chem. Chem. Phys.*, 2012, **14**, 2501–2507.
- 33 F. Cao, F. Donnarumma and K. K. Murray, *Analyst*, 2016, **141**, 183–190.
- 34 R. Shroff, K. Schramm, V. Jeschke, P. Nemes, A. Vertes, J. Gershenzon and A. Svatos, *Plant J.*, 2015, **81**, 961–972.
- 35 R. Verkerk, M. Schreiner, A. Krumbein, E. Ciska, B. Holst, I. Rowland, R. De Schrijver, M. Hansen, C. Gerhauser, R. Mithen and M. Dekker, *Mol. Nutr. Food Res.*, 2009, **53**, S219–S265.
- 36 J. W. Fahey, A. T. Zalcman and P. Talalay, *Phytochemistry*, 2001, **56**, 5–51.
- 37 M. Strohm, D. Kavan, P. Novak, M. Volny and V. Havlicek, *Anal. Chem.*, 2010, **82**, 4648–4651.
- 38 L. J. Song, J. J. Morrison, N. P. Botting and P. J. Thornalley, *Anal. Biochem.*, 2005, **347**, 234–243.

Electronic Supplementary Information for

**Enhanced Sensitivity and Metabolite Coverage with Remote Laser
Ablation Electrospray Ionization-Mass Spectrometry Aided by
Confined Coaxial Gas Flow**

Jarod A. Fincher,^a Andrew R. Korte,^a Brent Reschke,^b Nicholas J. Morris,^b Matthew J. Powell,^b and
Akos Vertes^{*,a}

^a *Department of Chemistry, W. M. Keck Institute for Proteomics Technology and Applications, The George Washington University,
Washington, DC 20052, USA*

^b *Protea Biosciences, 955 Hartman Run Road, Morgantown, WV 26505,*

** Corresponding author. E-mail: vertes@gwu.edu. Phone: +1 (202) 994-2717, Fax: +1 (202) 994-5873.*

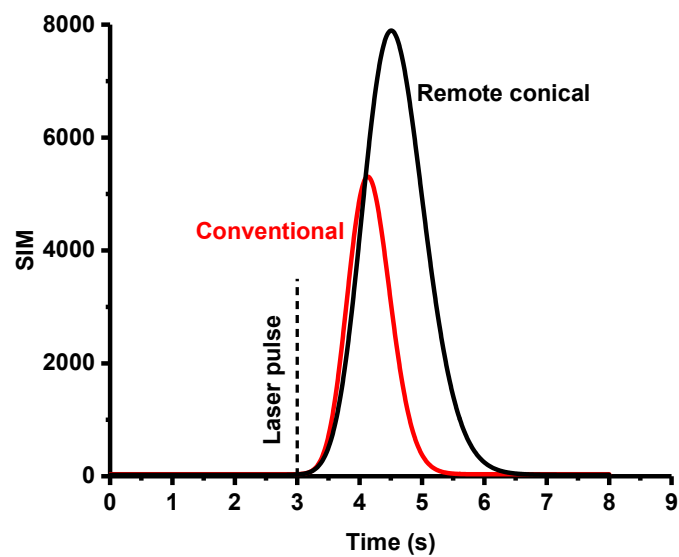


Figure S1: Signal profiles fitted by lognormal distributions from an ablation event in conventional LAESI-MS (red trace corresponding to verapamil molecular ion at m/z 455.29 from standard solution) and LAESI-MS in conical ablation chamber (black trace corresponding to disaccharide ion at m/z 381.06 from carrot tissue section).

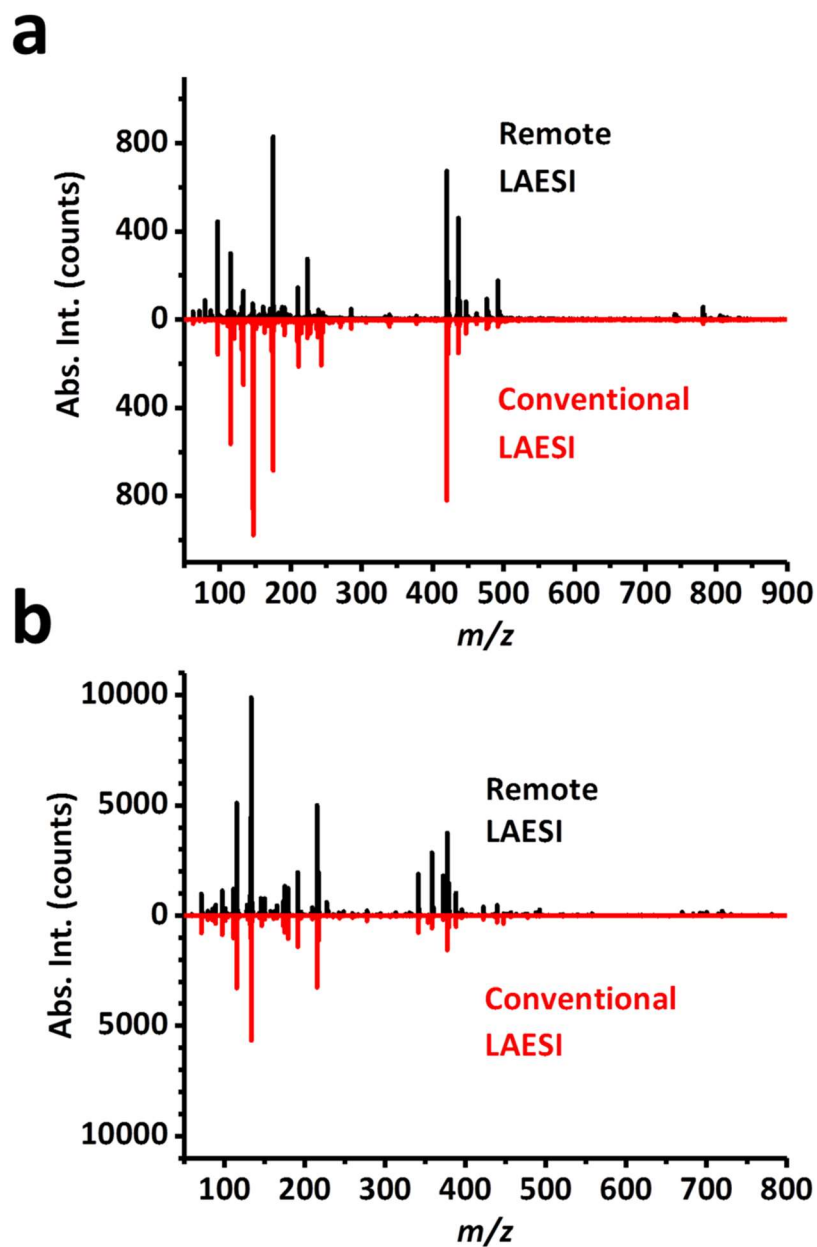


Figure S2: a) Negative ion mode mass spectra obtained from *Arabidopsis thaliana* leaves using remote LAESI-MS with a conical inner volume ablation chamber and conventional LAESI-MS. After deisotoping, 101 peaks were detected using remote LAESI-MS and 88 using conventional LAESI-MS. b) Negative ion mode spectra obtained from 60 μm thick Brussels sprout bud sections using remote LAESI-MS with a conical inner volume ablation chamber and conventional LAESI-MS. After deisotoping, 161 peaks were detected in remote LAESI-MS and 144 in conventional LAESI-MS.

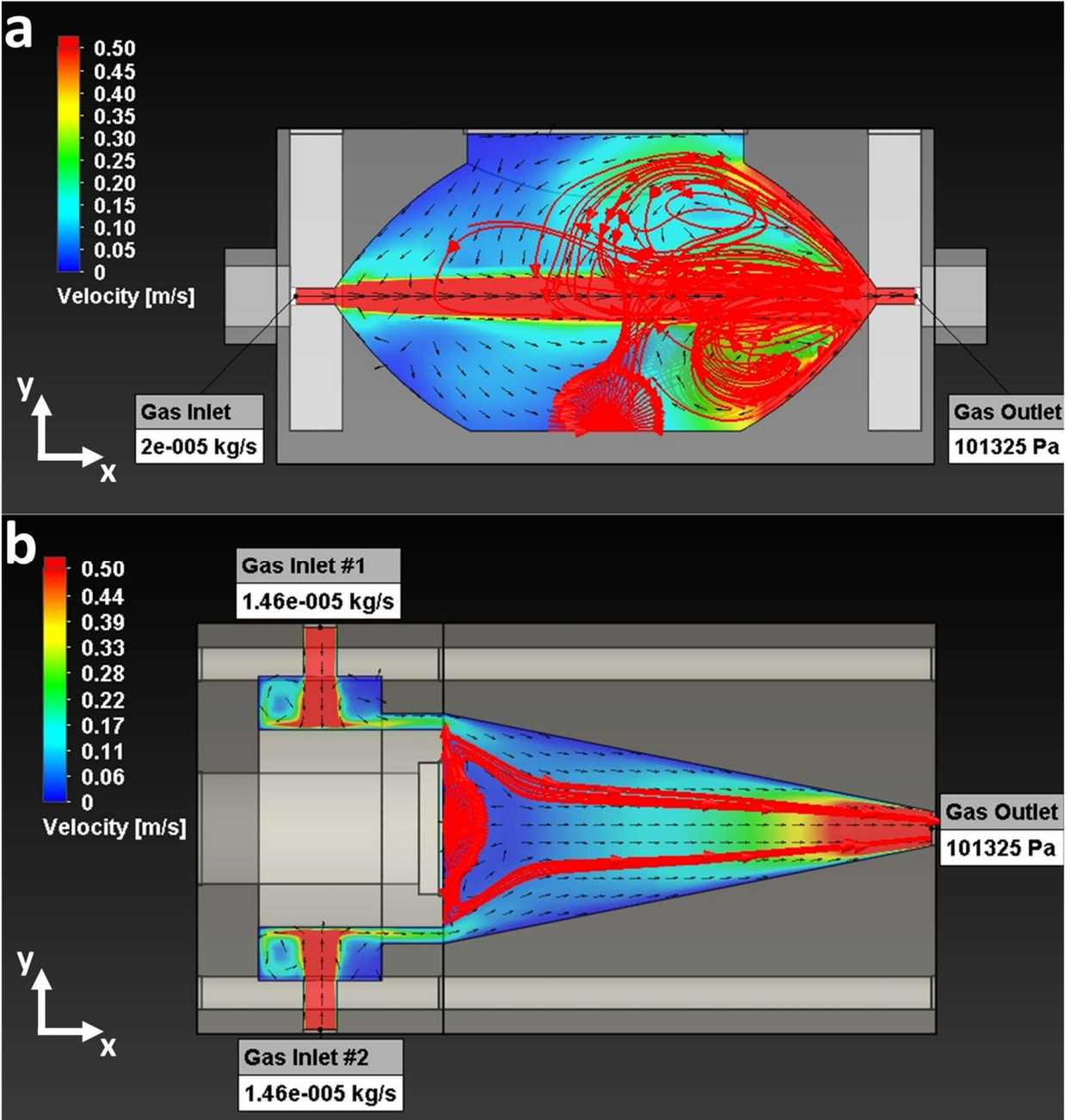


Figure S3: Overlay of particle trajectories (red traces) with carrier gas flow contour plots and black arrows for a) prolate spheroid ablation chamber and b) conical inner volume ablation chamber.

Table S1: Glucosinolates detected in 8-week old *Arabidopsis thaliana* plant leaf by conventional and remote LAESI-MS in negative ion mode. Glucosinolate identities were verified by tandem MS.

Compound Name	Chemical Formula	Measured <i>m/z</i>	Calculated <i>m/z</i>	Δm (mDa)
Glucoerucin	[C ₁₂ H ₂₃ NO ₉ S ₃ -H] ⁻	420.0447	420.0457	-1.0
Glucoraphanin	[C ₁₂ H ₂₃ NO ₁₀ S ₃ -H] ⁻	436.0406	436.0406	0.0*
Glucobrassicin	[C ₁₆ H ₁₉ N ₂ O ₉ S ₂ -H] ⁻	447.053	447.0532	-0.2
7-Methylthioheptyl glucosinolate	[C ₁₅ H ₂₉ NO ₉ S ₃ -H] ⁻	462.0932	462.0926	0.6
8-Methylthiooctyl glucosinolate	[C ₁₆ H ₃₁ NO ₉ S ₃ -H] ⁻	476.107	476.1083	-1.3
Neoglucobrassicin	[C ₁₇ H ₂₁ N ₂ O ₁₀ S ₂ -H] ⁻	477.0645	477.0638	0.7
Glucohirsutin	[C ₁₆ H ₃₁ NO ₁₀ S ₃ -H] ⁻	492.1042	492.1032	1.0

*This ion was used as an internal calibration point.

Table S2: Glucosinolates detected in 60- μ m-thick Brussels sprout bud tissue sections in conventional and remote LAESI-MS negative ion mode. Glucosinolate identities were verified by tandem MS.

Compound Name	Chemical Formula	Measured <i>m/z</i>	Calculated <i>m/z</i>	Δm (mDa)
Sinigrin	[C ₁₀ H ₁₇ NO ₉ S ₂ -H] ⁻	358.0272	358.0272	0.0*
Gluconapin	[C ₁₁ H ₁₉ NO ₉ S ₂ -H] ⁻	372.0438	372.0429	0.9
Progoitrin	[C ₁₁ H ₁₉ NO ₁₀ S ₂ -H] ⁻	388.0392	388.0372	2.0
Glucoiberin	[C ₁₁ H ₂₁ NO ₁₀ S ₃ -H] ⁻	422.029	422.0249	4.1
Glucobrassicin	[C ₁₆ H ₁₉ N ₂ O ₉ S ₂ -H] ⁻	447.053	447.0532	-0.2
Glucohirsutin	[C ₁₆ H ₃₁ NO ₁₀ S ₃ -H] ⁻	492.1049	492.1032	1.7

*This ion was used as an internal calibration point.